Combining continuous spatial and temporal scales for SGD investigations using UAV-based thermal infrared measurements

Ulf Mallast[1], Christian Siebert[1]

[1] Helmholtz Centre for Environmental Research -UFZ, T. Lieser Str. 4, Halle 06120, Germany

5 *Correspondence to*: Ulf Mallast (ulf.mallast@ufz.de)

Abstract. Submarine groundwater discharge (SGD) is highly variable in spatial and temporal terms due to interplay of several terrestrial and marine processes. While discrete in-situ measurements provide a continuous temporal scale to investigate underlying processes and thus accounts for temporal heterogeneity, remotely sensed thermal infrared radiation sheds light on the spatial heterogeneity as it provides a continuous spatial scale.

10 Here we report results of the combination of both, the continuous spatial and temporal scales, using the ability of an Unmanned Aerial Vehicle to hover above a predefined location and the continuous recording of thermal radiation of a coastal area at the Dead Sea (Israel). With a flight altitude of 65m above the water surface resulting in a spatial resolution of 13cm and a thermal camera (FLIRTau2) which measures the upwelling long-wave infrared radiation at 4Hz resolution we are able to generate a time sequence of thermal radiation images which allows us to analyse spatiotemporal SGD dynamics.

15 In turn, we are able to enhance focused SGD spots otherwise being camouflaged by strong lateral flow dynamics that may not be observed on single thermal radiation images. Plus, we show the spatiotemporal behaviour of a SGD induced thermal radiation pattern to vary in size and over time by up to 55% for focused SGDs and by up to 600% for diffuse SGDs due to different underlying flow dynamics. These flow dynamics even display a short-term periodicity in the order of 20 to 78 seconds for diffuse SGD which we attribute to an interplay of conduit maturity/geometry and wave setup.

20 ## 1 Introduction

Submarine groundwater discharge (SGD) is defined as "any and all flow of water on continental margins from the seabed to the coastal ocean" (Burnett et al., 2003). The definition already implies several shares of water with different origin contributing to SGD. Next to recirculated seawater it is also fresh groundwater of meteoric origin. The relative share of each water contribution depends on terrestrial and marine controls. Recharge amounts, aquifer permeability and hydraulic

25 gradients define the terrestrial groundwater contribution which may be the mayor SGD share in areas with high permeability such as karstic environments. In areas with low hydraulic gradients and low permeability the mayor SGD share shifts towards recirculated seawater driven by constantly changing hydraulic gradients that are caused by tidal or lunar cycles, storms or wave setup. In-situ measurements such as seepage meters, multilevel piezometer, tracers etc. possess the ability to discriminate between the shares and allow a linkage to the underlying processes since the investigated temporal scale is

continuous and ranges between daily to seasonal cycles (Taniguchi et al., 2003a; Michael et al., 2011). Yet, all cannot account for the spatial variability as the entity and interaction of terrestrial and marine controls lead to a highly variable SGD appearance in terms of discharge type (diffuse vs. focused), flow rates, spatial abundance (even over small spatial scales), mixing, and of its temporal behaviour (Michael et al., 2003; Taniguchi et al., 2003b; Burnett et al., 2006).

5 In contrast, remote sensing technology allows identifying and quantifying SGD over larger spatial scales without neglecting its spatial and partly even temporal variance or the need to extrapolate from in-situ measurements. Depending on the intended spatial scale utilized platforms differ between satellite (spatial coverage >10.000km²), airplane (spatial coverage >100km²), and lately unmanned aerial vehicle (hereafter UAV) systems (spatial coverage >0.1km²). From these systems the majority of all approaches measure thermal infrared radiation (hereafter thermal radiation/radiances) (a.o. Mejías et al., 2012;
10 Kelly et al., 2013; Mallast et al., 2013b; Schubert et al., 2014; Lee et al., 2016).

The principle is based on temperature contrasts between SGD water and ambient water at the sea-surface. These surface temperatures are directly proportional to emitted thermal radiation (see Stefan-Boltzman Law and assuming a rather similar emissivity for water), why thermal sensors allow identifying SGD through thermal radiation anomalies. This qualitative approach is expanded by few studies that use thermal anomalies to quantify SGD through a relation of anomaly (plume) size
15 to measured or modelled SGD rates (Kelly et al., 2013; Tamborski et al., 2015; Lee et al., 2016). Given a positive buoyancy of groundwater, the intriguing simplicity of these approaches is based on the momentum of discharging groundwater (Mallast et al., 2013a) and a potential deflection in the water body due to currents / wave action (Lee et al., 2016) or external forces (e.g. wind) (Lewandowski et al., 2013), and Newton's law of cooling (Vollmer, 2009). While the latter leads to a convective heat transfer between the discharging and the ambient water with an exponential adaption behaviour at the fringe
20 of the plume, the momentum and deflections are the forces defining the size and shape of the plume. In turn, it leads to positive relationship between plume size and discharge rate (Johnson et al., 2008; Mallast et al., 2013a; Lee et al., 2016) for parts of the plume not being deflected. Albeit the thoroughly clear practicability and numerous advantages in terms of spatial continuity and as a possible quantification approach, all studies rely on thermal radiation snapshots recorded at a certain instantaneous time.

25 Thus, in terms of scale, the advantage of remote sensing for SGD investigations is clearly the continuous spatial scale which allows deriving a clear picture of SGD abundance and quantity independent of its appearance and spatial variability. On the contrary, the advantage of in-situ measurements is explicitly the continuous temporal scale permitting a process understanding and elaborating on the drivers.

However, with the advent of UAVs and the ability of multi-copters as a type of UAVs to hover over a predefined location, it
30 becomes possibly to combine the continuous spatial and temporal scales. Consequentially the combination offers to investigate the spatiotemporal behaviour of SGD in a context and with a spatial and temporal resolution that was not possible

before. Here we report the results of such a study that uses a thermal camera system mounted beneath a multi-copter hovering above a predefined location to i) investigate the spatiotemporal variability of focused and diffuse SGD and ii) to outline additional values of the presented approach. The study is conducted at a site of the hypersaline Dead Sea, at which previously investigated submarine and terrestrial springs emerge. Existing hydraulic gradients in the discharging aquifers

5   and high density differences between ground- and lake water qualify the terminology SGD, which is usually bound to marine environments only.

2 Material and Methods

2.1 Study area

The study was conducted at known and pre-investigated SGD site (Ionescu et al., 2012; Mallast et al., 2013b; Siebert et al.,

10 2014) at the eastward side of the sedimentary fan of Wadi Darga located at the western coast of the Dead Sea (Fig. 1a, 1d and 1e).

2.1.1 Hydrogeological setting

Discharging groundwater at the study area is replenished in the Judean Mountains either through precipitation or flashfloods, which enter the Upper Cretaceous lime- and dolostone Judea Group Aquifers (JGA) and flow eastwards towards the Dead

15 Sea Transform (DST). The transition to the DST is marked by normal faults and block tectonics. Within the Graben, the Quaternary fluvio-lacustrine Dead Sea Group (DSG) is deposited in front of the Cretaceous rocks (Yechieli et al., 2010) and receives fresh groundwater through lateral flow from the JGA. The DSG consists of clastic sediments (gravel and sand) and stratified lacustrine sediments (clay minerals, aragonite, gypsum, halite) (Yechieli et al., 1995). Groundwater flow occurs through several subaquifers with different groundwater levels and chemical compositions due to the alternations of coarse

20 and fine strata (Yechieli et al., 2010). In addition, due to the high solubility of evaporitic minerals and microbial activity, dissolution cavities develop, representing zones of higher hydraulic conductivity and thus preferential flowpaths. They lead to a karst-like behaviour of groundwater movement (Magal et al., 2010; Ionescu et al., 2012). However, due to the continuous drop of the Dead Sea water level of ~1.3m per year, the entire flow system is highly dynamic resulting in different degrees of maturity of its karstic parts. As a result, discharge rates, locations and composition of springs along the

25 lake shore vary intensely (Burg et al., 2016). It is hence proposed, observable highly variable chemical compositions of discharging groundwater even within meters range are an expression of the maturity of the karst system. The less mature the conduits are, the larger the ratio between wetted surface and volume, resulting in highly variable concentrations between diffuse SGD (less mature karst system) and focused SGD (mature karst system).

2.1.2 Submarine groundwater discharge and onshore spring characteristics

At the investigation site, focused SGD occurrences were mapped in 2011 and 2012 by SCUBA divers and hydrochemically investigated. Based on their findings groundwater emerges from mature karst-like underground cavities down to depths of

5   30m below water table (Ionescu et al., 2012; Mallast et al., 2014).

From these cavities groundwater emerges as focused SGD. Subsequently, density differences between SGD water (1.00–1.19g·cm^{-3}) and Dead Sea brine (1.234g·cm^{-3}) trigger a continuous positive buoyancy (buoyant jet) of the emerging groundwater towards the lakes sea surface. Within the water column and alongside the buoyant jet develop considerable turbulences entraining ambient Dead Sea water. Thus the ascending water represents a mixture of fresh and brackish water.

10   Once the ascending water reaches the lakes sea surface it develops a radially orientated flow away from its jet centre causing circular-like pattern. These patterns are partly visually observable as shown in Mallast et al. (2014) at the Dead Sea or in various other cases (Swarzenski et al., 2001).

Apart from focused SGD, diffuse SGD occurs at the investigation site as well either in various depths below water surface (Ionescu et al., 2012) or at the shoreline. At the study area one diffuse SGD site exists directly at the shoreline (Fig. 1e). The

15   discharge seems to occur over a length of approximately 20-25m parallel to the shoreline and was only detectable visually through the occurrence of schlieren in the lake brine. Sampling of this water was not possible as neither the true origin nor any discharge was identifiable that was unaffected by seawater. However, five more springs exist onshore that have been sampled.

2.1.3 Hydrologic and atmospheric setting

20   At the time of emergence SGD water temperatures are 21-31.5°C. During the time of investigation the Dead Sea had a skin temperature of ~21°C providing a temperature maximum difference of 10.5°C between warmer groundwater and cooler ambient Dead Sea water. Wind speeds amounted to 0.87m·s−1 (±0.16) approaching from SE to E (80°-128°). Occurring waves, which may influence SGD size and shape, had a frequency of 3-7 seconds with estimated wave heights <15cm. During the flight, cloud free conditions and thus homogenous solar radiation existed being equally reflected at the sea-

25   surface within the entire recorded area.

2.2 Material

The general approach to investigate the spatiotemporal thermal radiation variability induced by SGD consist of hovering with an UAV (multicopter - model: geo-X8000) above a pre-defined SGD spot (Fig. 1c) over a time period of several

minutes. The flight was conducted on Feb., 10th 2016 between 12:43 and 12:50 a.m.. During that flight the UAV is equipped with a thermal system comprising i) a long-wave infrared camera core (FlirTau2), which is an uncooled VOx Microbolometer with a 19mm lens and a 640x512 focal plane array (FLIR® Systems (2016)) and ii) a ThermalCapture module - radiometry module and image grabber (TeAx Technology, 2016)). The system senses LWIR radiation in the spectral range of 7.5 - 13.5μm with a sensitivity of <50mK and captures LWIR (thermal) 14 bit images at a frame rate of 9Hz from which only every 5th frame is exportable (approx. 4-5Hz) deduced after own tests. The core was calibrated prior to the flight using an internal flat-field-corrector.

The hovering position is 31.576516N/35.415775E with a flight altitude of 65m above Dead Sea level. Due to the GPS controlled nature of the UAV the hovering position displays a certain spatial variability which is according to the flight log ±1.5m in horizontal dimension and ±1.75m in vertical dimension. Position and altitude are chosen (i) due to Israeli regulatory framework and ii) to cover land and water in equal shares. The latter is important for the co-registration of each recorded image to a selected master image (see section 2.3) in order to correct the spatial variability of the UAV and the sensor during hovering and to determine the position accuracy of the co-registration which is based on two aluminium reflectors placed directly on the shore (Fig. 1b and 1c).

2.3 Data processing

Thermal radiance image recording with 4-5 Hz results in a total of 670 images recorded within a time span of 167 seconds. Each image displays thermal radiances emitted by the surface. According to the Stefan-Boltzman Law these radiances are directly proportional to the existing surface temperatures and thus are the basis for the present study. Yet, due to the UAV position variability while hovering above the pre-defined flight position, the mapped image footprint is not congruent for each image but varies spatially in the same magnitude as the position variability.

To overcome the varying footprint we define the first image of the set as master image and all remaining ones as slave images (Fig. 2). Subsequently all slave images are co-registered onto the master image using an intensity based image registration. The registration uses a similarity transformation which considers translation, rotation and scaling as possible factors induced by the UAV position variability and thus the non-congruent footprints. It was chosen due to the facts that the short-time differences between images will not cause nonlinear geometric differences while especially the land and placed reflectors represent those rigid parts needed to calculate a reliable transformation matrix. The matrix similarity between input matrix (master image) and transformation matrix (each slave image) is determined using a mean square metric that was iteratively optimized through a regular step gradient descent until a minimum step length of 1e-05 was reached.

The so obtained co-registration accuracy of all images, evaluated based on the positions of both reflectors, has a RMSE of 0.58 pixel (1 pixel = 13 cm) with a mean of 0.5 pixel and a standard deviation of 0.3 pixel (see attachment Fig. S 1).

As a consequence of the co-registration process, we reduced the image sizes to a common footprint extent represented by all images. The so obtained image size amounts to 561x376 pixel which are used during subsequent steps. Onto all co-registered

images we then applied a manually derived land mask and normalized the radiance values of the remaining water area using a z-score normalization to account for potential global solar radiation differences that may occur over the time of investigation and would affect the result. The so obtained processed image set consist of 670 images (hereafter frames) resembling a total time period of ~167 seconds.

2.4 Delineation of diffuse and focused SGD spots

Since SGD at the investigated site consists of focused SGD occurring offshore and diffuse SGD occurring at the land-water interface we used different approaches to extract relevant discharge spots separately to finally pursue the intended temporal investigations. Given the assumption of a thermally stabilized area over time induced by focused SGD (Mallast et al., 2013b; Siebert et al., 2014) we calculate the thermal variance per pixel of the entire frame set. The resulting low variance areas represent focused SGD sites. These sites are extracted using a subjective variance threshold of <0.019. To eliminate extraction artefacts we apply a morphological closing and deletion of objects smaller than 150 pixel to obtain the low variance area representing focused SGD sites only.

In contrast, diffuse SGD discharges less water and has a smaller momentum which inevitably leads to a smaller area ($\sim10^1$-10^2 cm perpendicular to the coastline) along the shoreline that is thermally stabilized. Yet, although being thermally stabilized, several direct forces such as breaking waves and currents influence the same area and thus the resulting thermal radiation pattern on the sea surface. These factors lead to rather high variances compared to focused SGD flow. Unfortunately, a similar variance can be expected from ambient areas likewise being influenced by highly dynamic flow field induced by waves, currents and discharge. As a consequence we delineate diffuse SGD from a single frame (frame 210 – not shown) in which thermal radiation patterns induced by high discharge rates are clearly detectable (first image in Fig. 3). Analogously to the focused SGD sites we applied a subjective threshold of >2.5 (normalized radiation) to extract discharge induced thermal patterns and eliminate extraction artefacts using a morphological closing to clean extracted pattern objects followed by the deletion of objects smaller than 150 pixel to focus on larger patterns only.

2.5 Spatiotemporal analyses

The likewise conducted temporal analysis includes (i) a spatiotemporal analysis to identify spatial variability of both thermal radiance patterns induced by SGD and (ii) a periodicity analysis to reveal possible reoccurring temporal discharge patterns of single SGDs. To explore the spatiotemporal behaviour of diffuse and focused SGD spots, we construct transects across the maximum extents of each extracted SGD spot as we expect here the most pristine patterns. Along each transect, normalized thermal radiances per frame are extracted, filtered using a 1D 9th-order median filter to reduce the white noise portion and finally plotted, highlighting the spatiotemporal behaviour for each spot.

For the periodicity analysis we use an autocorrelation function, which measures the self-similarity of a signal (Tzanetakis and Cook, 2002). If discharge occurs regularly, it causes a periodic signal, which is expressed as significant peak (above or below 95% confidence interval) in the autocorrelation function. These investigations are pursued at specific single pixels,

which are the respective midpoint of each transect as we expect the clearest and most pristine discharge induced thermal pattern signals at these locations, for both SGD types.

2.5 Water chemistry and inverse geochemical modelling

Physicochemical parameters (temperature, density, pH, electrical conductivity) of all the above mentioned focused SGD but also onshore springs were measured in the field using WTW 350i and Mettler Toledo density meter. The sampling procedure for water samples in order to analyse major element concentrations of the discharging waters followed the procedure described in detail in Ionescu et al. (2012). Generally, samples for anion and cation analyses were filtered (0.22 µm CA filters), separately filled in HDPE bottles and stored cool. Cation samples were immediately acidified and later analysed applying ICP-AES. Anions were analysed using ion chromatography and bicarbonate by Gran titration.

The individual water/rock interactions, which lead to the chemical composition of the respective groundwaters in the springs were inversely modelled applying Phreeqc and Pitzer thermodynamic database. The latter was applied since the sediment body through which the fresh groundwaters migrate is soaked with interstitial brine, which admixes to the fresh groundwater. Reactive solid phases were selected on the base of the abundant easily soluble minerals (halite, aragonite and gypsum) in the sedimentary succession. Ion exchange on clay minerals was enabled. Modelling results were selected on the base of probability and lowest sum of residuals.

2 Material and Methods

It is a proven fact that SGD influences the sea surface temperature and thus the thermal radiances and is clearly detectable given a sufficient contrast between groundwater and sea/lake water temperature and a certain discharge volume/ momentum (Johnson et al., 2008; Lee et al., 2016). Our results confirm this fact as diffuse SGD induces thermal radiance patterns with values >1 (higher temperatures) that is clearly visible in the first frame (Fig. 3) and spatially coincides with our field observations. Yet, the single thermal radiance image suggests the diffuse discharge to occur in two distinguishable patterns.

The first pattern is a coastal fringe of 35m length and of ~10 pixel (1.3m) width, showing elevated normalized thermal radiance (NTR) values >1. This distribution along the shoreline exceeds the visual results of ca 20m by a factor of two and suggests a homogeneously distributed, low velocity and low rate discharge of warmer groundwater that partly emerges onshore and partly directly at the water/land interface (1st frame in Fig. 3).

The second, seemingly dominant pattern is characterized by NTR values >1, but in contrast to the first, it consists of distinctive counter-rotating vortex pair (CVP) flow structures (Cortelezzi and Karagozian, 2001), discernible based on the mushroom shape, with length axes between ~20 to ~46 pixel (2.6m-6.0m). The cause appears to be a focused and lateral jet-like discharge at four locations (1st frame in Fig. 3). Plumes, caused by both discharge forms, are subsequently deviated towards N-NE.

Focused SGD with an expected circular to elliptic shape as observations shown in Mallast et al. (2014) and Swarzenski et al. (2001) suggest, are not clearly visible from the single frame (one thermal radiance image) only. At the upper and at the left end of the single frame (1st frame in Fig. 3) three half-circular patterns with NTR values between -0.6 and 0 foreshadow focused SGD spots, which coincide with in-situ observed and sampled focused SGD spots 11/120, 11/121 and 12/382. Yet, from the thermal radiation perspective clear spatial indications for more than these three SGD-sites are missing.

Given the assumption of SGD to thermally stabilize thermal radiance variation at the sea surface over time, as shown for satellite images (Schubert et al., 2014; Oehler et al., 2017), we integrate several frames (thermal radiance images) to enhance the abovementioned focused SGD spots and to reveal further ones.

The thermal radiation variance of 10, 50 and 100 frames (integration of ~2.5, 12.5 and 25 sec. respectively) already indicates thermally stable (variance values <0.2) and thermally labile areas (variance values ≥0.2). However, with larger integration times of 300 and 670 frames (integration of ~75 and 176 sec. respectively), the three abovementioned focused SGD spots appear plus two additional SGD spots in the upper part of the resulting variance image (lower right image, Fig.3) which spatially coincide with in-situ observed focused SGD sites 11/101, and 11/102. In the following, we focus on the three largely complete focused SGD spots 1 to 3 (Fig. 3). These three focused SGD spots exhibit variance values <0.019 and elliptical (1st spot) to circular (2nd and 3rd spot) shapes at the sea-surface underlined by the individual length/width ratios (Fig.4). The lowest variance values and therefore the thermally most stable areas locate at the southern end of the 1st and 2nd SGD spot and on the northern end of the 3rd SGD spot. Thermally indicated surface areas vary between 4.1 and 28.7 m² albeit the similar spring depth of 13-20 m.

3.1 Spatiotemporal behaviour of discharge induced thermal radiance patterns

While the previous variance analysis highlights thermally stable and labile areas useful for identifying SGD spots it allows statements concerning the spatiotemporal discharge behaviour of each SGD spot only conditionally. These information will be derived through the introduction of transects (see left column of Fig.5 and Fig.6) constructed across the maximum extent of each extracted focused and diffuse SGD spot as we expect here the most pristine patterns representative for each spot.

3.1.1 Spatiotemporal behaviour of focused SGD spots

The middle column of Fig.5 shows the time sequences of NTR values along each SGD transect. Furthermore, SGD spot boundaries are indicated (white lines =maximum gradients of each transect profile), which provide an orientation for the spatiotemporal behaviour of each spot. The focus is set on the area in between the boundaries representing the area in which SGD governs the thermal radiation distribution. In case of the 1st focused SGD spot, the location is rather stable with its centre between transect pixel 18 and 23 (spatial shift of <0.65m). In contrast, its boundaries are highly dynamic resulting in a varying distance between 20 and 31 pixel (~2.6m to 4.0m respectively; for 90% of the data) and thus a change of 55% (Table 1). This dynamic partially follows a certain trend during which both boundaries (white lines) show a synchronous directional change over a certain period (e.g. frame 150-400). Within the SGD spot, NTR values peak around the transect centre and

decrease towards both boundaries. This peak is higher during the first 300 frames with NTR values ~0.24 and decreases slightly between frames 300 to 500 to values of 0.08 before it increases to values around 0.18 for the remaining frames.

The centre of the 2nd focused SGD spot shifts between transect pixel 40 to 45 (<0.65m), indicating similar stable conditions, while the boundary behaviour slightly differs from the 1st focused SGD spot. The lower boundary is rather stable fluctuating around transect pixel 70, whereas the upper boundary describes on average a wave-like change between frames 1 and 300 before displaying a stable fluctuation around transect pixel 20. The resulting diameter of the 2nd focused SGD spot is therefore between 43 and 60 pixel (~5.59 to 7.8m; for 90% of the data) and thus show a change of 39% (Table 1).

Compared to 1st focused SGD spot, the absolute peak values of the 2nd focused SGD spot of -0.26 and their general trend over time are lower. They display a rather random behaviour over all frames with the exception of frames 485 to 520 during which the peak values (around -0.17) are higher.

The location of the 3rd focused SGD spot, which centres between transect pixel 15 to 20 is as stable as the latter. The spot's boundaries are stable during the first 200 frames during which they display a synchronous directional change similar to the 1st focused SGD spot. For the remaining frames, the lower boundary is highly dynamic and totally random while the upper is rather stable with less fluctuation until frame 350 before it also starts to become highly dynamic with random change. The resulting boundary distance between the first 200 frames is between 18 to 21 pixel (~2.34m to 2.73m respectively; for 90% of the data) and thus resemble a change of 16% (Table 1). The peak values of -0.08 to 0.06 resemble those of the 1st and to a lesser extent those of the 2nd focused SGD spot. Over time, they exhibit a similar random behaviour over all frames with the exception of frames 485 to 520 during which the peak values are higher with values of ~0.06.

3.1.2 Spatiotemporal behaviour of diffuse SGD spots

Analogous to the focused SGD spots, the middle column of Fig. 6 shows time sequences of the NTR values along the transects of each diffuse SGD spot to illuminate the spatiotemporal discharge behaviour. Apparent for the 1st, 2nd, and 3rd diffuse SGD spots are higher NTR values > 4 for a constant transect length of 5-8 pixel (~0.65m-1.02m) starting at the shoreline. Only the 4th diffuse SGD spot exhibits no constantly elevated NTR values over the entire observation time close the shoreline. All spots have in common to show outburst-like events during which NTR values > 3 occur. Between all, the onsets and influence lengths of theses outburst events vary. While for the first spot the average influence length reaches 20 pixel (=2.60m) for NTR values >3, the average lengths of the second is 33 pixel (=4.29m), the third has a length of 20 pixel (2.60m) and the fourth only 7 pixel (0.91m). Consequentially the percentage change of the influence length axis is between 150% for the first and third diffuse SGD spot, amounts to 266% for the second spot and reaches up to 600% for the fourth spot.

3.2 Periodicity analysis

The previous spatiotemporal behaviour already pointed at a certain recurrence pattern of the observed thermal radiation but lacked a distinct statement on whether or not it contains a significant periodicity and thus a dominating forcing inducing it. In order to provide a clear and temporally mostly pristine discharge signal we analyse its temporal pattern based on a single

5   pixel of each transect (midpoint of the transect) using a temporal autocorrelation analysis (see right column in Fig. 5 and Fig.6 respectively).

3.2.1 Periodicity of focused SGD spots

Temporal autocorrelation of the 1st focused SGD spot distinctively differs from the 2nd and 3rd focused SGD spots. The 1st spot shows a small but significant negative autocorrelation of -0.25 between lags (frames) 268 and 367 (~64-92 seconds)

10   indicating a recurring pattern and hence a certain periodicity (Fig. 5). This observation matches the aforementioned peak value shift from 0.24 to 0.08 at the same frame region. The 2nd focused SGD spot shows a small positive autocorrelation of 0.21 at lag (frame) 80, while remaining peaks vary in both directions, but below the confidence intervals. Both facts are distinctively different to the autocorrelation of the 1st focused SGD spot, but resemble the autocorrelation function of the 3rd SGD spot whose peaks are exclusively insignificant and reflecting no periodicity indication.

15   **3.2.2 Periodicity of diffuse SGD spots**

Time sequence plots (middle column in Fig. 6) already indicate a regular recurrence of thermal radiation values. This behaviour is underlined by the temporal autocorrelation of all diffuse SGD spots, which show a significant temporal autocorrelation that occurs at different lags and mostly with different intensities (Fig. 4). While the 1st diffuse SGD spot exhibits only one significant period at lag 81 (~20 seconds), the 2nd spot shows two, one at lag 81 and a second one at lag

20   247 (~62 seconds). Despite the spatial proximity of ~5m to the ones before, the 3rd diffuse SGD spot shows a different temporal autocorrelation with one significant peak at lag 143 (~36 seconds). Similarly different is the 4th spot, which exhibits two peaks at lag 198 (~50 seconds) and lag 314 (~78 seconds). All plots in the right column contain a reference autocorrelation function of a pixel close at the source point at the shoreline (transect pixel three). This reference clearly shows a high-frequent behaviour unlike the ones described before (except for the last diffuse SGD spot).

25   **3.3 Water chemistry and inverse geochemical modelling**

The sampled focused SGD and onshore springs display a temperature between 21 and 31.5°C. Though the groundwater of both focused SGD and onshore springs originates from the same freshwater JGA they discharge brackish water with salinities (TDS) ranging between 4.87 g/l and 26.0 g/l with the tendency to be on average less saline onshore (TDS=12.8 g/l) compared to the focussed SGD (TDS=20.1 g/l). The inverse geochemical modelling results indicate halite, aragonite and

30   gypsum to be the most important minerals in solution, though ion exchange on clay minerals plays a significant role.

However, although discharge locations are very close, the amount of dissolved halite (0-0.01 mol/kg H2O), aragonite (0-0.004 mol/kg H2O) and gypsum (0-0.02 mol/kg H2O) vary significantly between the different springs (Table 2). Translated into cavitation rates, the different branches of the groundwater system, which feed the individual springs, dissolve 59–1.552 cm3 of halite, aragonite and gypsum per cubic meter of through-flowing groundwater.

4. Discussion

The high spatial and temporal resolutions of the thermal radiation data clearly show a highly dynamic setting with various discharge locations, patterns, and forces. Analysing the spatiotemporal behaviour of each SGD spot independent of its type reveals striking details: i) it enhances focused SGD patterns otherwise being camouflaged by strong lateral flow dynamics and sheds light on crossflow influences, ii) the spatiotemporal behaviour shows a thermal SGD pattern size variation over time of up to 55% for focused SGDs and 600% for diffuse SGDs due to different flow dynamics and iii) it reveals a periodicity for diffuse SGD. We discuss these aspects in the following and outline possible driving forces or causes and conclude with general remarks to the presented approach and transferability.

4.1 Enhancing focused SGD

Deriving clear SGD indications from single frames such as in Fig. 3 might be non-trivial especially in a highly dynamic system as the one presented. For the present case we suggest the following causes to be relevant:

(i)   lateral flow dynamics induced by diffuse discharge with higher temperatures (see point (ii)) govern the investigated area and superimpose thermal radiance signals from vertical flow of focused SGD as mentioned in Mallast et al. (2013a), and

(ii)   entrainment of ambient water during the turbulent ascent (buoyant jet) of groundwater to the sea-surface (Jirka, 2004) leads to a consequential adaption of temperature and thus the emitted thermal radiance,

(iii)   potential groundwater discharge fluctuation with possibly very small to stagnant discharge rates, as described in Ionescu et al. (2012) for the presented site, at the moment of recording which lead to no traceable thermal radiance signal from SGD at the sea surface.

However, the abovementioned possible relevant causes have in common to be dynamic in spatial and temporal terms. Thus, accounting for the fact of a thermal stabilization at the sea surface as a consequence of a continuous discharge of equally tempered groundwater (Siebert et al., 2014) reveals thermally stable area induced by SGD that might otherwise be not detectable. The thermal stabilization is accompanied by the interplay of fluid movements (lateral vs. vertical flow kinetics) and thus resulting and developing water surface geometries (wave structures) e.g. at the interface of opposing water flows. Surface geometries have an effect on the recorded thermal radiances due to the directional dependence of the surface emissivity (Norman and Becker, 1995; Cheng and Liang, 2014). Wave fronts for example with surfaces being orthogonal to the sensor (0°) would have highest thermal radiance values. As the angle to the sensor increases, recorded thermal radiances decrease although the sea surface-temperature is the same (Cheng and Liang, 2014). Thus the temporal effects through a

thermal stabilization and changing surface geometries as a consequence of flow dynamics are the two governing drivers which allow to easily detecting focused SGD through the integration of thermal radiation over longer time periods. According to our findings the thermal radiance variance over a period of 25 seconds (100 frames) already provides a sufficient basis to outline SGD areas (Fig. 2). Integrating over longer time periods even emphasizes SGD areas, which

5   consequently confirms the thermal radiance stabilization over time at the sea surface of a SGD-affected area (Siebert et al., 2014).

Apart from enhancing focused SGD occurrences, the shape of the focused SGD variance pattern at the sea surface along with location of the lowest variance values (thermally most stable area) gives an indication of SGD emergence locations and the deflection of the resulting vertical plume until it reaches the sea surface. None of the three are perfectly circular which would

10   refer to an uninfluenced positive buoyancy of discharging water and a SGD emergence directly beneath the centre of the variance pattern (Jirka, 2004). Instead, they all are more or less elliptic with lowest variance values at the southern (1st and 2nd SGD spot) and at the northern ends (3rd spot). The remarkable elliptic shape of the 1st SGD spot implies a crossflow from south causing a northward deflection of the vertical SGD plume and an elliptic shape of the horizontal plume pattern at the sea surface (Akar and Jirka, 1995). The same northward deflection with less pronounced elliptic shapes exhibit the 2nd

15   and 3rd SGD spot. This deflection is most likely induced by flow dynamics as a consequence of diffuse SGD. Since the location of the diffuse SGD spots, especially those with distinctively periodic events with higher discharge rates (Fig. 4), is directly SSW and shows the same northward horizontal plume orientation, we suggest this discharge to be the driving force for the deflection.

4.2 Spatiotemporal behaviour of SGD patterns

20   The variance image provides an average representation of all SGD spots, which are especially useful for reliable size/discharge comparison purposes between SGD spots and likewise allow outlining SGD spots. However, as the previous section already points out, all are subject to external forces such as currents, waves but also internal discharge dynamics influencing resulting pattern shape and size characteristics of the thermal radiance pattern over time.

For focused SGD the observed thermal radiance pattern sizes (distance between boundaries) over time show a spatial

25   variation between 16% (=2.3m for the first focused SGD spot) and 55% (=4.0m for the third focused SGD spot). The variance is clearly a result of occurring lateral flow dynamics constantly influencing the pattern on the sea surface. Yet, the influence is anisotropic in space and time as the lateral flow dynamics are dominated by waves coming from the East, the interaction of horizontal SGD plumes on the sea surface (e.g. 2nd and 3rd focused SGD) as described in Teamah and Khairat (2015), but moreover the strong lateral flow dynamics (crossflow) induced by the discharge impulses of diffuse SGD that in

30   the following is deflected to the NE. The interplay and constant temporal changes lead to an asynchronous boundary movement for most of the observed SGD induced thermal radiance patterns that it is only partly changing to a synchronous movement as for the 1st and 3rd focused SGD spot during the first 200 frames. During this time only one force seems to dominate the dynamic, causing the synchronous behaviour.

The SGD induced thermal radiation pattern size variation is different for the observed diffuse SGD spots. While three out of four spots constantly influence an area of 5-8 pixel (~0.65-1.04m) along the shoreline, outburst-like events change the influence length perpendicular to the shoreline between 150-600% and between ~0.60-4.29m. The constant influence reflects a continuous diffuse discharge with lower discharge rates. The latter however clearly shows a focused flow with intermittent

5   higher discharge rates. Higher discharge rates induce a higher momentum and consequentially increases the influenced area off the discharge spot. In turn it reveals karst conduits to exist already close to the shoreline and next to diffuse SGD. The intermittency with a seemingly reccurring temporal pattern however points at a steady interplay of different forces that is subject to the next section.

4.3 Periodicity of diffuse SGD

10   For focused SGD spots, we could not reveal a significant periodicity, either because of the limited observation length or because no periodicity exists. For diffuse SGD spots the temporal autocorrelation analysis reveals significant periodicities. The periodicity of discharge rate events varies significantly among given spots between 20 to 78 seconds (right column of Fig. 4). Primarily, it provides a further example of the high temporal discharge variability even over small spatial scales which, normally, is due to tides or wave-setup that change hydrostatic pressure conditions (Taniguchi et al., 2003b; Burnett

15   et al., 2006). For the present case, tidal influences are irrelevant as the tidal cycles do not exist at the study site. Wave influence on the other hand cannot be excluded per se. However, most likely it is not the main cause since observed wave frequency of 3-7 seconds would cause high-frequency discharge intermittency of the same magnitude. Precisely this high frequency is observable in the autocorrelation graphs of Fig. 4 close to the shoreline (transect pixel 3). Yet, it likewise proves the minor wave influence on the main discharge events with an observed frequency that is up to 10 magnitudes larger. Along

20   with the focused discharge nature, it rather points at an interplay of wave-setup and a geometry effect within conduits of groundwater flow as underlying mechanism as described for karst areas in Smart and Ford (1986). Discharge behaviour in this case depends on the maturity and geometric formation of the conduit network, is therefore highly anisotropic, heterogeneous, and features a rapid flow (Surić et al., 2015). Especially anisotropy and heterogeneity can likewise be observed for the discharge behaviour of all SGD spots since neither discharge onset nor periodicity agrees among the

25   individual spots even though their spatial location is within 10m distance.
Plus, through the existence of several subaquifers as described in Yechieli et al. (2010) conduits can develop through the fuzzy dissolution of easily soluble minerals aragonite, gypsum, and halite contained in the sediment. These conduits are assumed to be less mature close to the shoreline, as the fresh-saltwater interface is moving lake-wards with dropping lake level and the subsequently dropping groundwater tables. Thus, in these areas the time of freshwater being in contact with

30   dissolvable sediment is short which leads to initial karstification status. However, due to the fuzziness of the process, even in this initial karstification area, the cavitation rates vary leading to different degrees of conduit maturity. Consequentially, it is thoroughly possible that an initial anisotropic karst system exists onshore and especially around the shoreline. This system is certainly less developed as the one described for focused SGD spots in Ionescu et al. (2012) yet similar anisotropic. In

interaction with the wave setup, we suggest the initial karst system to be the cause for the different onsets and influence areas for the observed outburst-like events.

4.3 General remarks

The hovering of the UAV over a predefined location and the sensing of thermal radiation at a rate of 4-5Hz allows
5 combining the continuous spatial with the continuous spatial scale. Thus it is possible to provide detailed and high resolution information on SGD dynamics but also on external forces influencing it. Despite the short total observation time of the present study it shows a temporal discharge behaviour in the range of 101-102 seconds. Classical in-situ measurements however usually have measuring intervals of 10^1-10^2 minutes (Cable et al., 1997; Mulligan and Charette, 2006; Michael et al., 2011) and thus differ by the order of one magnitude. These intervals could not reflect the observed short-term discharge
10 dynamics. Moreover, the spatiotemporal continuous results also provide indication on suitable and unsuitable sampling sites in spatial terms. E.g. with the clear indication on where diffuse SGD occurs and where exactly the transition between diffuse SGD with a focused SGD nature is, indicates proper sampling sites for each of them, that could not be done with a subjective selection of sampling sites. Thus, applying the presented approach before pursuing in-situ sampling which includes the selection of proper sampling sites and sampling intervals is undoubtedly advantageous.
15 It is likewise advantageous for SGD monitoring and especially SGD quantification purposes. Recalling from the introduction, the basis for SGD quantification is the size of thermal radiance patterns (plumes) in most studies (Kelly et al., 2013; Mallast et al., 2013a; Tamborski et al., 2015; Lee et al., 2016). The presented results show a spatial variation of 150-600% for diffuse SGD which indicates the possible uncertainty that underlies a quantification based on single thermal infrared images.
20 In this context the question arises on the transferability of the presented approach. In general we propose the approach to be applicable to other areas with diffuse or focused SGD since the method requires an UAV with a mounted thermal camera system only and some rigid points/area within the covered footprint to allow a proper co-registration of all frames. Recommendable is furthermore a temperature difference of groundwater and ambient water allowing a clear differentiation.

5. Conclusion

25 Hovering with a UAV over a predefined location recording thermal radiances at a temporal resolution of 4-5Hz is a novel application technique combining continuous spatial and temporal scales. Based on the combination we enhance focused SGD patterns otherwise being camouflaged by strong lateral flow dynamics that may not be observed on single thermal radiation images. We furthermore show the spatiotemporal behaviour of a SGD induced thermal radiation pattern to vary in size and over time by up to 55% for focused SGDs and by up to 600% for diffuse SGDs due to different underlying flow
30 dynamics. We want to emphasize this aspect as it is important for SGD monitoring and especially SGD quantification purposes which rely on single thermal radiation images and thus temporal snapshots which may not provide the entire picture. And lastly we are able to reveal a short-term periodicity in the order of 20 to 78 seconds for diffuse SGD which we

attribute to an interplay of conduit maturity/geometry and wave setup. The observed periodicity differs by the order of a magnitude to classical in-situ measurement intervals, which would not be able to detect the temporal behaviour we observe. Since SGD, independent of its type, is highly heterogeneous in space and time, as we have also shown in our study, we suggest, where possible, to include the presented approach before any in-situ sampling to identify proper sampling locations and intervals. In that way SGD investigations, especially in systems with complex flow, will be able to optimize sampling strategies and will possibly improve their results.

Acknowledgements: This work was financed by the DESERVE Virtual Institute, funded by the Helmholtz Association of German Research Centers (VH-VI-527) and a scholarship from German Federal Ministry of Education and Research (YSEP97). Personal thanks are addressed to Yossi Yechieli and Gideon Baer (both Geological Survey of Israel) for the kind support, the warm welcome and unconditional assistance before and during the exchange of UM including the logistical help. Meteorological Data were provided by KIT (Jutta Metzger).

References

Akar, P. J., and Jirka, G. H.: Buoyant spreading processes in pollutant transport and mixing part 2: Upstream spreading in weak ambient current, Journal of Hydraulic Research, 33, 87-100, 1995.

Burg, A., Yechieli, Y., and Galili, U.: Response of a coastal hydrogeological system to a rapid decline in sea level; the case of Zuqim springs – The largest discharge area along the Dead Sea coast, Journal of Hydrology, 536, 222-235, https://doi.org/10.1016/j.jhydrol.2016.02.039, 2016.

Burnett, W. C., Aggarwal, P. K., Aureli, A., Bokuniewicz, H., Cable, J. E., Charette, M. A., Kontar, E., Krupa, S., Kulkarni, K. M., Loveless, A., Moore, W. S., Oberdorfer, J. A., Oliveira, J., Ozyurt, N., Povinec, P., Privitera, A. M. G., Rajar, R., Ramessur, R. T., Scholten, J., Stieglitz, T., Taniguchi, M., and Turner, J. V.: Quantifying submarine groundwater discharge in the coastal zone via multiple methods, Science of The Total Environment, 367, 498-543, 10.1016/j.scitotenv.2006.05.009, 2006.

Cable, J., Burnett, W., Chanton, J., Corbett, D., and Cable, P.: Field evaluation of seepage meters in the coastal marine environment, Estuarine, Coastal and Shelf Science, 45, 367-375, 1997.

Cheng, J., and Liang, S.: Effects of Thermal-Infrared Emissivity Directionality on Surface Broadband Emissivity and Longwave Net Radiation Estimation, IEEE Geoscience and Remote Sensing Letters, 11, 499-503, 10.1109/LGRS.2013.2270293, 2014.

Cortelezzi, L., and Karagozian, A. R.: On the formation of the counter-rotating vortex pair in transverse jets, Journal of Fluid Mechanics, 446, 347-373, 2001.

FLIR® Systems: Tau® 2 Uncooled Cores: http://www.flir.com/cores/display/?id=54717, access: 16.12.2016, 2016.

Ionescu, D., Siebert, C., Polerecky, L., Munwes, Y. Y., Lott, C., Häusler, S., Bižić-Ionescu, M., Quast, C., Peplies, J., Glöckner, F. O., Ramette, A., Rödiger, T., Dittmar, T., Oren, A., Geyer, S., Stärk, H.-J., Sauter, M., Licha, T., Laronne, J. B., and de Beer, D.: Microbial and Chemical Characterization of Underwater Fresh Water Springs in the Dead Sea, PLoS ONE, 7, e38319, 10.1371/journal.pone.0038319, 2012.

5 Jirka, G. H.: Integral model for turbulent buoyant jets in unbounded stratified flows. Part I: Single round jet, Environmental Fluid Mechanics, 4, 1-56, 2004.

Johnson, A. G., Glenn, C. R., Burnett, W. C., Peterson, R. N., and Lucey, P. G.: Aerial infrared imaging reveals large nutrient-rich groundwater inputs to the ocean, Geophysical Research Letters, 35, L15606 15601-15606, 10.1029/2008gl034574, 2008.

10 Kelly, J. L., Glenn, C. R., and Lucey, P. G.: High-resolution aerial infrared mapping of groundwater discharge to the coastal ocean, Limnology and Oceanography: Methods, 11, 262-277, 10.4319/lom.2013.11.262, 2013.

Lee, E., Yoon, H., Hyun, S. P., Burnett, W. C., Koh, D. C., Ha, K., Kim, D. j., Kim, Y., and Kang, K. m.: Unmanned aerial vehicles (UAVs)-based thermal infrared (TIR) mapping, a novel approach to assess groundwater discharge into the coastal zone, Limnology and Oceanography: Methods, 14, 725-735, 10.1002/lom3.10132, 2016.

15 Lewandowski, J., Meinikmann, K., Ruhtz, T., Pöschke, F., and Kirillin, G.: Localization of lacustrine groundwater discharge (LGD) by airborne measurement of thermal infrared radiation, Remote Sensing of Environment, 138, 119-125, 2013.

Magal, E., Weisbrod, N., Yakirevich, A., Kurtzman, D., and Yechieli, Y.: Line-Source Multi-Tracer Test for Assessing High Groundwater Velocity, Ground Water, 48, 892-897, 10.1111/j.1745-6584.2010.00707.x, 2010.

Mallast, U., Schwonke, F., Gloaguen, R., Geyer, S., Sauter, M., and Siebert, C.: Airborne Thermal Data Identifies
20 Groundwater Discharge at the North-Western Coast of the Dead Sea, Remote Sensing, 5, 6361, 2013a.

Mallast, U., Siebert, C., Wagner, B., Sauter, M., Gloaguen, R., Geyer, S., and Merz, R.: Localisation and temporal variability of groundwater discharge into the Dead Sea using thermal satellite data, Environmental Earth Sciences, 1-17, 10.1007/s12665-013-2371-6, 2013b.

Mallast, U., Gloaguen, R., Friesen, J., Rödiger, T., Geyer, S., Merz, R., and Siebert, C.: How to identify groundwater-caused
25 thermal anomalies in lakes based on multi-temporal satellite data in semi-arid regions, Hydrol. Earth Syst. Sci., 18, 2773-2787, 10.5194/hess-18-2773-2014, 2014.

Mejías, M., Ballesteros, B. J., Antón-Pacheco, C., Domínguez, J. A., Garcia-Orellana, J., Garcia-Solsona, E., and Masqué, P.: Methodological study of submarine groundwater discharge from a karstic aquifer in the Western Mediterranean Sea, Journal of Hydrology, 464–465, 27-40, 10.1016/j.jhydrol.2012.06.020, 2012.

30 Michael, H. A., Lubetsky, J. S., and Harvey, C. F.: Characterizing submarine groundwater discharge: a seepage meter study in Waquoit Bay, Massachusetts, Geophysical Research Letters, 30, 2003.

Michael, H. A., Charette, M. A., and Harvey, C. F.: Patterns and variability of groundwater flow and radium activity at the coast: A case study from Waquoit Bay, Massachusetts, Marine Chemistry, 127, 100-114, http://dx.doi.org/10.1016/j.marchem.2011.08.001, 2011.

Mulligan, A. E., and Charette, M. A.: Intercomparison of submarine groundwater discharge estimates from a sandy unconfined aquifer, Journal of Hydrology, 327, 411-425, 2006.

Norman, J. M., and Becker, F.: Terminology in thermal infrared remote sensing of natural surfaces, Remote Sensing Reviews, 12, 159-173, 10.1080/02757259509532284, 1995.

5 Oehler, T., Eiche, E., Putra, D., Adyasari, D., Hennig, H., Mallast, U., and Moosdorf, N.: Timing of land-ocean groundwater nutrient fluxes from a tropical karstic region (southern Java, Indonesia), Hydrol. Earth Syst. Sci. Discuss., 2017, 1-18, 10.5194/hess-2017-621, 2017.

Schubert, M., Scholten, J., Schmidt, A., Comanducci, J. F., Pham, M. K., Mallast, U., and Knoeller, K.: Submarine Groundwater Discharge at a Single Spot Location: Evaluation of Different Detection Approaches, Water, 6, 584-601, 2014.

10 Siebert, C., Rödiger, T., Mallast, U., Gräbe, A., Guttman, J., Laronne, J. B., Storz-Peretz, Y., Greenman, A., Salameh, E., and Al-Raggad, M.: Challenges to estimate surface-and groundwater flow in arid regions: The Dead Sea catchment, Science of the Total Environment, 485, 828-841, 2014.

Smart, C., and Ford, D.: Structure and function of a conduit aquifer, Canadian Journal of Earth Sciences, 23, 919-929, 1986.

Surić, M., Lončarić, R., Buzjak, N., Schultz, S. T., Šangulin, J., Maldini, K., and Tomas, D.: Influence of submarine

15 groundwater discharge on seawater properties in Rovanjska-Modrič karst region (Croatia), Environmental Earth Sciences, 74, 5625-5638, 10.1007/s12665-015-4577-2, 2015.

Swarzenski, P. W., Reich, C. D., Spechler, R. M., Kindinger, J. L., and Moore, W. S.: Using multiple geochemical tracers to characterize the hydrogeology of the submarine spring off Crescent Beach, Florida, Chemical Geology, 179, 187-202, https://doi.org/10.1016/S0009-2541(01)00322-9, 2001.

20 Tamborski, J. J., Rogers, A. D., Bokuniewicz, H. J., Cochran, J. K., and Young, C. R.: Identification and quantification of diffuse fresh submarine groundwater discharge via airborne thermal infrared remote sensing, Remote Sensing of Environment, 171, 202-217, http://dx.doi.org/10.1016/j.rse.2015.10.010, 2015.

Taniguchi, M., Burnett, W. C., Cable, J. E., and Turner, J. V.: Assessment methodologies for submarine groundwater discharge, in: Land and Marine Hydrogeology, edited by: Taniguchi, M., Wang, K., and Gamo, T., Elsevier, Amsterdam, 1-

25 23, 2003a.

Taniguchi, M., Burnett, W. C., Smith, C. F., Paulsen, R. J., O'Rourke, D., Krupa, S. L., and Christoff, J. L.: Spatial and temporal distributions of submarine groundwater discharge rates obtained from various types of seepage meters at a site in the Northeastern Gulf of Mexico, Biogeochemistry, 66, 35-53, 10.1023/B:BIOG.0000006090.25949.8d, 2003b.

TeAx Technology: Thermal Capture http://thermalcapture.com/category/products/recordingsolutions/, access: 16.12.2016,

30 2016.

Tzanetakis, G., and Cook, P.: Musical genre classification of audio signals, IEEE Transactions on speech and audio processing, 10, 293-302, 2002.

Vollmer, M.: Newton's law of cooling revisited, European Journal of Physics, 30, 1063, 2009.

Yechieli, Y., Shalev, E., Wollman, S., Kiro, Y., and Kafri, U.: Response of the Mediterranean and Dead Sea coastal aquifers to sea level variations, Water Resoures Research, 46, W12550 12551-12511, 10.1029/2009wr008708, 2010.
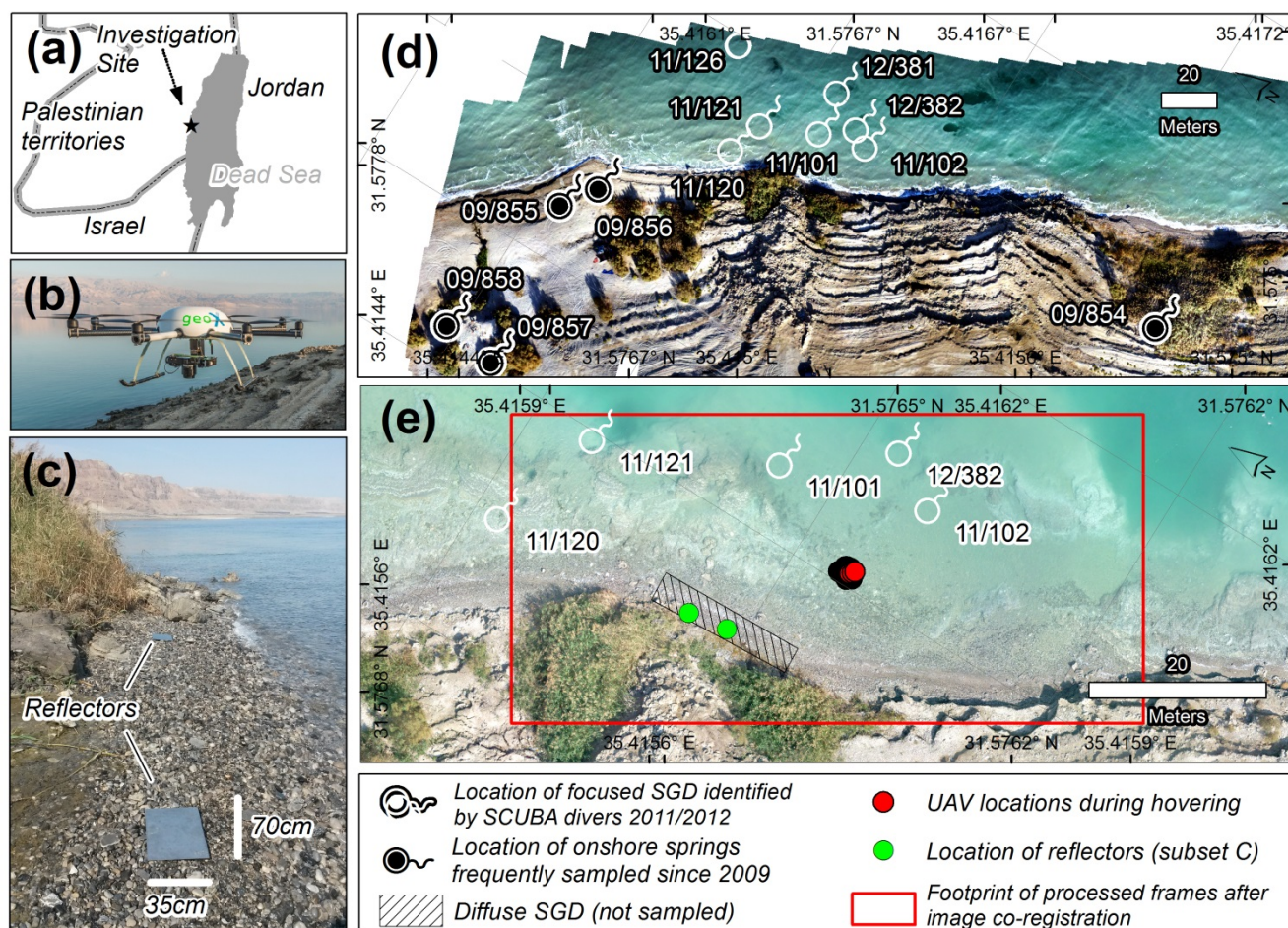
Figure 1: Location of the study area in at the Dead Sea (A), photo of the UAV used during the study (B), photo of both reflectors at the covered coastline section (C), distribution of focused SGD spots identified and sampled by divers in the years 2011 and 2012 and onshore springs which have been sampled frequently since 2009 (D), and aerial photograph from February 10th, 2016 at 12:11 p.m. local time of the covered area along with UAV positions during hovering, location of reflectors, the footprint of the processed frames after co-registration described in section 2.3 and locations of observe diffuse SGD (E).
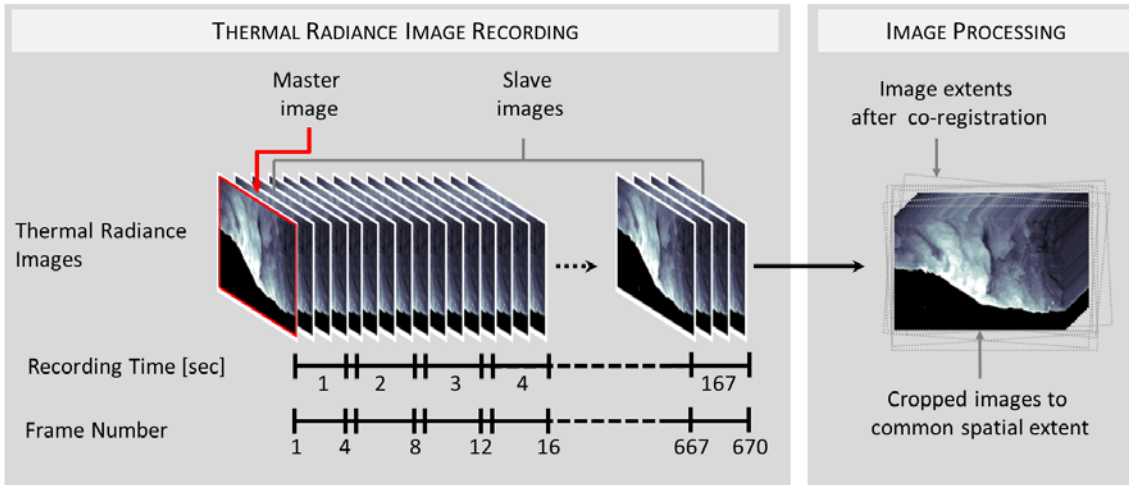
Figure 2: Graphical illustration of image recording and image pre-processing applied during the presented approach.
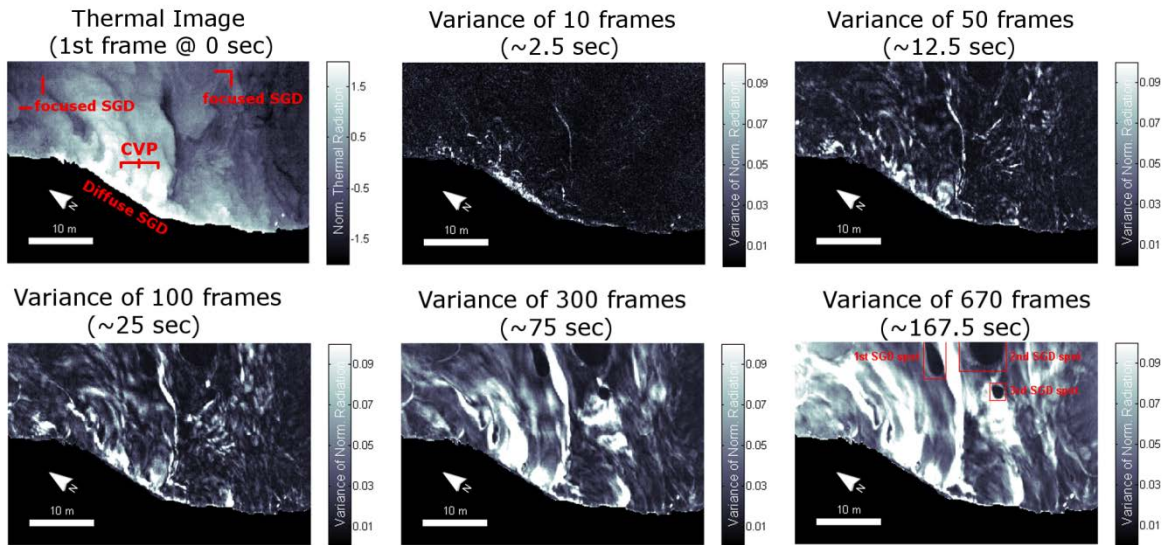
Figure 3: Variance of normalized thermal radiances over time starting with a normalized thermal radiance image (1st frame) showing indications of focused SGD spots, diffuse SGD and counter rotating vortex pairs (CVP) as indication of a focused flow within the diffuse SGD area (upper left). The following panels show the integration of 10, 50, 100, 300, and 670 frames as variance per pixel. The final image (lower right) shows three delineated focused SGD spots (red boxes) indicated through variance values <0.019.
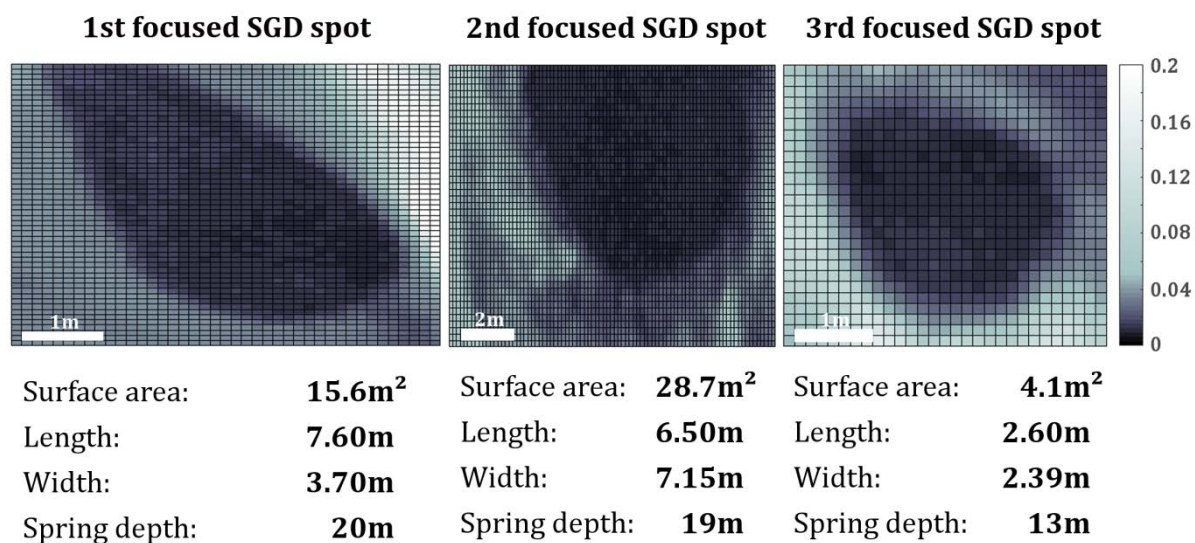
Figure 4: Spatial characteristics of the three focused SGD spots elaborated and focused on during the present study.
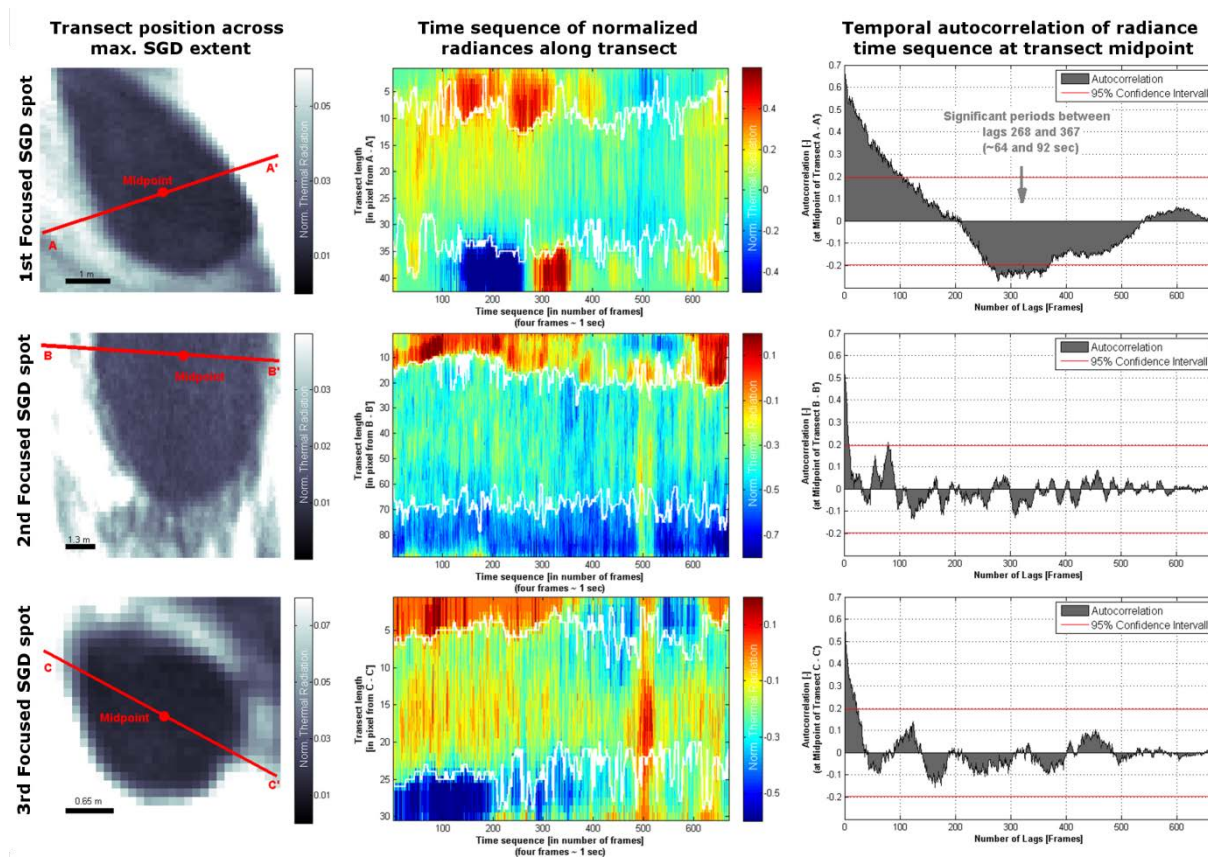
Figure 5: Analyses of spatiotemporal behavior and potential periodicity of SGD spots are presented. The first column shows transects across the maximum extent and midpoint position of SGD spot (subsets correspond to the red boxes shown in Fig. 4; note that the spatial scale varies between each spot indicated through the scale bar at the lower left of each subset). The middle column shows the normalized radiance values along transects over time. The white lines indicate the boundary of the focused SGD spots. The third column shows the temporal autocorrelation of the normalized radiance values along the entire frame set (time sequence) obtained at the midpoint of transect as described in section 2 to detect possible periodicities.
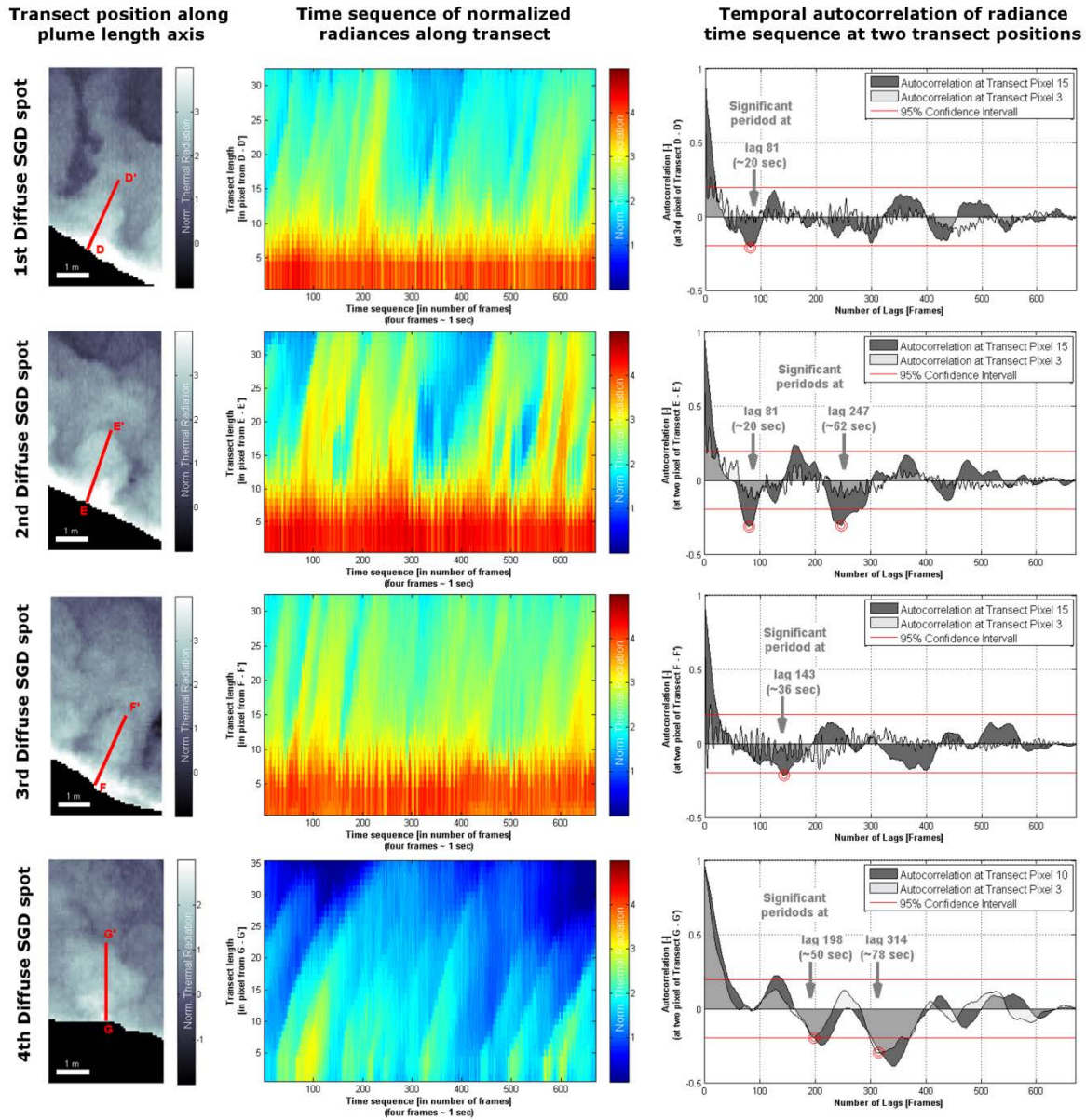
Figure 6: Analyses of spatiotemporal behavior and potential periodicity of diffuse SGD spots are presented. The first column shows transects across the maximum extent and midpoint position of diffuse SGD spots (note that the spatial scale varies between each spot indicated through the scale bar at the lower left of each subset). The middle column shows the normalized radiance values along transects over time. The third column shows the temporal autocorrelation of the normalized radiance values along the entire frame set (time sequence) obtained at the midpoint of transect. Those points reflect the clearest and mostly pristine discharge signals (the larger value). As reference we show the third transect pixel as well to outline the wave influence on the periodicity.

Table 1: Summary of values characterizing the spatiotemporal behaviour of each focused SGD spot

SGD spot	Boundary distance*			Peak Values** (standard deviation)	Distinctive feature
	[in pixel]	[in meter]	[in %]		
1st	20-31	2.60-4.03	55.0	0.08 - 0.24 (0.11)	Higher peak values during frames 100-300 and 500-670 and lower during frames 301-499
2nd	43-60	5.59-7.80	39.5	-0.17- -0.26 (0.09)	Exceptional peak values during frames 485-520
3rd	18-21	2.34-2.73	16.7	-0.08 - 0.06 (0.07)	Exceptional peak values during frames 485-520

* For 90% of the data
** Mean of the maximum values per frame over time

Table 2: Water chemistry of all sampled focused SGD and onshore spring, along with the result from the inverse geochemical modeling and the volumetric calculation

	analytical results											Modelling results											volumetric calculation*			
	T	pH	Na	K	Ca	Mg	Cl	SO4	HCO3	TDS	density	interstitial brine	fresh water	halite	aragonite	gypsum	MgX2	CaX2	NaX	KX	CO2(g)	Sum residuals	halite	aragonite	gypsum	sum
	[°C]	[-]				[mmol/l]				[g/l]	[g/cm3]	[kg]	[mol H2O]					[mol/kgw]						[cm3/m3 H2O]		
interstitial brine	35.6	5.38	1717	192	356	1651	6701	3.37	1.64	345	1.23															
onshore springs																										
Ter_Sp #1 09/854	27.9	7.20	40.9	5.34	9.54	28.6	129	1.62	3.80	7.3	1.00	0.012	54.9	0.0123	0.0017	0.0017	0	0	-0.0020	0.0020	0.0023	0.21	359.5	59.5	125.7	544.7
Ter_Sp #2 09/855	28.5	7.12	129	14.8	48.1	116	429	19.8	4.00	26.0	1.00	0.049	52.8	0	0.0017	0.0201	0	0	0	0	0.0022	0.91	0	59.4	1493.0	1552.4
Ter_Sp #3 09/856	28.1	7.16	89.3	9.01	23.6	68.4	261	8.74	3.96	15.6	1.00	0.028	53.9	0	0.0019	0.0087	-0.0066	0	0.0132	0	0.0020	0.61	0	65.3	649.4	714.7
Ter_Sp #4 09/857	27.6	7.11	140	11.5	28.0	87.5	363	9.30	3.80	21.2	1.00	0.039	53.3	0	0.0017	0	-0.0244	0.0058	0.0371	0	0.0021	0.24	0	59.0	0.0	59.0
Ter_Sp #5 09/858	27.6	7.48	35.6	4.31	9.6	26.3	110	1.66	4.23	6.4	1.00	0.011	54.9	0.0071	0.0020	0.0016	-0.0006	0	0	0.0013	0.0022	0.88	208.3	69.5	119.8	397.6
average												0.023		0.0061	0.0021	0.0050										
submarine springs																										
Sub_Sp #1 11/120	29.6	7.25	68.9	9.61	26.8	82.9	270	7.13	5.03	15.8	1.00	0.030	53.8	0	0.0025	0.0071	0.0042	0	-0.0083	0	0.0025	0.39	0	85.5	527.1	612.6
Sub_Sp #2 10/30	28.0	6.75	464	56.7	137	502	1693	25.5	2.77	9.5	1.00	0.201	44.3	0	0	0.0011	0.0271	0	0	0	0	2.65	0	0	79.8	79.8
Sub_Sp #3 12/366	31.5	7.27	45.2	6.19	12.0	37.9	154	2.28	4.57	8.7	1.00	0.015	54.7	0.0056	0.0021	0.0024	0	-0.0008	0	0.0017	0.0027	-0.84	163.4	73.3	177.3	414.0
Sub_Sp #4 11/126	30.0	7.37	26.2	3.77	6.92	21.1	81.4	1.22	4.43	4.9	1.00	0.008	55.1	0.0051	0.0021	0.0012	0	-0.0007	0	0.0015	0.0023	0.35	150.0	71.6	88.0	309.6
Sub_Sp #5 11/101	24.0	7.16	70.4	9.51	17.6	59.3	216	3.50	7.79	12.8	1.00	0.022	54.3	0.0109	0.0036	0.0034	0	-0.0015	0	0.0031	0.0043	0.35	319.3	122.3	254.8	696.5
Sub_Sp #6 11/102	26.6	7.24	77.9	9.90	19.3	65.8	239	3.76	6.86	13.9	1.00	0.025	54.1	0.0125	0.0032	0.0037	0	-0.0014	0	0.0028	0.0037	0.42	365.6	110.3	273.8	749.7
Sub_Sp #7 11/121	21.0	7.08	125	14.5	44.7	130	415	10.7	4.28	24.8	1.00	0.048	52.8	0	0.0018	0	-0.0160	0.0160	0	0	0.0027	0.54	0	62.4	0	62.4
average												0.038		0.0124	0.0022	0.0053										

* volumetric calculation bases on the molar volume of halite (29.24 cm3/mol); aragonite (34.17 cm3/mol) and of gypsum (74.29 cm3/mol)